

PAPER

CrossMark
click for updatesCite this: *RSC Adv.*, 2014, 4, 40464

Assessing the effect of flow fields on flocculation of kaolin suspension using microbial flocculant GA1

Zhaohui Yang,^{*ab} Zhou Wu,^{ab} Guangming Zeng,^{ab} Jing Huang,^{ab} Haiyin Xu,^{ab} Jing Feng,^{ab} Peipei Song,^{ab} Min Li^{ab} and Like Wang^{ab}

In this work, the effect of flow fields on flocculation efficiency in a kaolin suspension using microbial flocculant GA1 (MBFGA1) was studied. The flow fields were controlled *via* mechanical mixing of a Rushton turbine in a fully baffled flocculation reactor and simulated by a three-dimensional Computational Fluid Dynamic (CFD) model. Good agreement between experimental and simulated results confirmed the validity and applicability of the CFD model. By integrating flocculation tests with CFD simulations, it was shown that the impeller with different speeds generated different flow fields, and hence offered different efficiencies for flocculation. Flow fields of rapid mixing at 400 rpm then slow mixing at 80 rpm, which formed the largest flocs ($538 \pm 18 \mu\text{m}$), achieved the optimum flocculation efficiency, *i.e.* the lowest residual turbidity ($3.03 \pm 0.10 \text{ NTU}$) and the maximum flocculation rate ($98.2 \pm 0.8\%$). The two-loop flow pattern associated with the distribution of velocity magnitude, local shear rate and turbulent kinetic energy provided an improved understanding of flow behaviors within the reactor. Additionally, charge neutralization and adsorption bridging were proposed as the main flocculation mechanisms of MBFGA1.

Received 5th May 2014
Accepted 27th August 2014

DOI: 10.1039/c4ra04101a

www.rsc.org/advances

1. Introduction

In modern water treatment technology, flocculation has been a long-established and well-known method of drinking water purification as well as sewage treatment.¹ As ineffective flocculation results in poorer quality feed water to downstream treatment processes, potentially jeopardising treated water quality and increasing operational costs, flocculation turns out to be a fairly important component of the overall suite of water treatment systems.² Generally, there exist two main aspects governing the efficiency of flocculation: physicochemical conditions and hydrodynamic conditions. Physicochemical conditions are related to the flocculant type and dosage, particle concentration, solution pH, and so on.³ Hydrodynamic conditions depend on both the geometry of the flocculation reactor in which the process is performed and the impeller speed and type.⁴

In terms of physicochemical conditions, the flocculant type possesses an important status during the flocculation process.¹ With the advantages of high-efficiency, non-toxicity and biodegradability over traditional flocculants, microbial flocculants (MBFs) have shown a great potential in industrial applications and attracted much attention recently.^{5–11} Most of the

investigations on MBFs concentrate on the screening of microorganisms, culture conditions, characterization of MBFs, and flocculation properties.^{9–11} Nevertheless, the effect of flow fields, *i.e.* hydrodynamic conditions within the flocculation reactor, on flocculation performance of MBFs is rarely involved. In general, the flocculation process consists of two stages. The first stage is the rapid dispersal of the flocculant into the wastewater followed by an intense agitation, which is commonly defined as rapid mixing, and the second stage is slow mixing at the flocculation step which is in charge of the growth of flocs.^{4,12} Previous reports have proved that flow fields of rapid mixing and slow mixing exhibit significant control over the effectiveness of flocculation.^{4,13,14} It is becoming increasingly important to evaluate the role of flow fields in the flocculation performance of MBFs.

With the introduction of Computational Fluid Dynamics (CFD) technique, modern CFD software make it possible to predict fluid flow, heat and mass transfer, chemical reactions and other related phenomena by solving a set of appropriate mathematical equations.² Recently, Samaras *et al.* carried out the CFD-based simulations, instead of expensive post-construction field tests, of flow fields in the full scale flocculation reactor and presented the dominant mechanism for the actual successful operation of the flocculation system.¹⁵ A quantitative analysis between floc growth/breakage and hydrodynamics can also be made by CFD simulations to improve the flocculation efficiency. Bridgeman *et al.* combined CFD and jar test data for a specific raw water and coagulant dose and the

^aCollege of Environmental Science and Engineering, Hunan University, Changsha, 410082, PR China. E-mail: yzh@hnu.edu.cn; Fax: +86 0731 88822829; Tel: +86 0731 88822829

^bKey Laboratory of Environmental Biology and Pollution Control (Hunan University), Ministry of Education, Changsha 410082, PR China

breakage threshold found, then a proposed flocculator could be modelled using CFD to determine the likelihood of floc breakage *via* analysis of the velocity gradients distribution within the vessel.¹⁶ The CFD investigation on flocculation conducted by Prat and Ducoste demonstrated the influence of the type of impeller on the spatial heterogeneity for the steady-state floc size and on the transient spatial evolution of the mean floc size.¹⁷ Consequently, performing a CFD study to figure out the flow characteristics within the reactor provides useful insights into the design/optimization of flocculation processes.¹⁵ Proceeding from actual engineering, CFD visualization and analysis eliminate the painful realization that a system is inefficient after installation.¹⁸ Visualization of fluid velocity vectors, streamlines, shear rate and turbulent kinetic energy can help the researcher understand the mixing mechanisms and identify possible problems in advance. At the present time, utilization of CFD to simulate flow fields in the flocculation reactor is still in its infancy.

As a kind of MBFs, MBFGA1 is harvested from the fermentation liquid of *Paenibacillus polymyxa* GA1.⁶ In this work, MBFGA1 was used for flocculation of kaolin suspension in a lab-scale flocculation reactor. The objective was to assess the effect of flow fields in the reactor on flocculation efficiency of MBFGA1 by integrating experimental investigations with CFD simulations. A series of flocculation tests were performed and a three-dimensional CFD model with a standard k - ϵ model was employed to simulate flow characteristics of the reactor. In addition, the flocculation mechanisms of MBFGA1 were also discussed.

2. Materials and methods

2.1. Reagents

The kaolin was chemically pure grade (Sanpu Chemicals, China), and its suspension was prepared at the concentration of 3 g L^{-1} . CaCl_2 , analytically pure grade (Sanpu Chemicals, China), was prepared at the concentration of 10 g L^{-1} . The pH was adjusted by NaOH and HCl, which were prepared at the concentration of 0.5 mol L^{-1} .

2.2. Bacteria strain and culture conditions

GA1, flocculant-producing strain CCTCC M206017, which was identified as *Paenibacillus polymyxa* by 16S rDNA sequence and its biochemical and physiological characteristics, was screened from the soil collected in the Yuelu Mountain Changsha, China.⁶ The seed medium was prepared as follows: peptone 10.0 g, beef extract 3.0 g and NaCl 5.0 g were added into 1 L distilled water with the pH adjusted to 7.0. The steam sterilization lasted 30 min at $121 \text{ }^\circ\text{C}$. After the inoculation of the seed medium, the GA1 was cultured on the roundabout shaker at 150 rpm and $30 \text{ }^\circ\text{C}$ for 24 h. The fermentation medium was prepared by dissolving sucrose 40.0 g, yeast extract 4.0 g, K_2HPO_4 5.0 g, KH_2PO_4 2.0 g, NaCl 0.1 g and MgSO_4 0.2 g into 1 L distilled water with the pH adjusted to 7.0. The steam sterilization lasted 30 min at $115 \text{ }^\circ\text{C}$. This cultivated process was divided into two stages. In the first 24 h, the medium was incubated at $30 \text{ }^\circ\text{C}$ and

was shaken at 150 rpm. In the following 48 h, the rotating speed of shaker was decelerated to 100 rpm and the temperature was decreased to $25 \text{ }^\circ\text{C}$. After 72 h of cultivation, the fermentation liquid with 15.56 g L^{-1} effective components was stored at $4 \text{ }^\circ\text{C}$, and it would be utilized directly in the flocculation tests.

2.3. Flocculation tests and analysis

2.3.1. Flocculation tests. As shown in Fig. 1(a), a lab-scale flocculation reactor with a Rushton turbine was designed for the flocculation of kaolin suspension dosed with MBFGA1. Provided that $D = 50 \text{ mm}$ for the impeller diameter, the other dimensions such as reactor diameter (T), liquid height (H), and width of each baffle (B) can be determined with $T = 3D$, $H = T$, and $B = T/10$. The impeller was centrally fixed 50 mm above the bottom of the reactor.

The pH of kaolin suspension was adjusted to 8.0. The dosages of CaCl_2 and MBFGA1 were optimized to $4 \times 10^{-3}\%$ (w/w) and $4.34 \times 10^{-3}\%$ (w/w), respectively. Then CaCl_2 and MBFGA1 were added into 2.5 L kaolin suspension (3 g L^{-1}) in the reactor, orderly. The flocculation test was divided into two stages. The first stage began with 1 min rapid mixing at five different impeller speeds, *i.e.* 200, 300, 400, 500 and 600 rpm, after adding CaCl_2 and MBFGA1. The second stage with 10 min slow mixing was conducted at six different impeller speeds of 50, 60, 70, 80, 90 and 100 rpm, respectively. After the two stages, the mixture went through gravity settlement procedure for 30 min, and then the upper phase and flocs were used for the experimental tests. The influence of flow fields in the reactor on flocculation was systematically investigated in terms of the key parameters, including the floc size, residual turbidity, flocculating rate and zeta potential of the flocculation system. All the batch experiments were carried out in triplicate.

2.3.2. Floc size analysis. For Reynolds numbers less than 1.0, viscosity is the predominant force governing the settling process. The settling velocity (u_p) of spherical particle is given by eqn (1):

$$u_p = g(\rho_p - \rho_w)d_p^2/(18\mu) \quad (1)$$

where ρ_p and ρ_w are the density of floc and water, respectively; g is acceleration due to gravity; μ is dynamic viscosity and d_p is the diameter of floc.¹⁹

Assuming that flocs are spherical particles with the same density, we can put forward a conclusion that flocs in various diameters will differ in settling velocity. According to this theory, a transparent rectangular container ($17 \times 2 \times 60 \text{ cm}$) was applied to separate the flocs huddling together. And a CCD camera was placed on the base of the container where the flocs were separated completely, thus ensuring the camera to capture each of the flocs clearly. A black background, at low level of reflection, was also needed to provide high-quality images. The diameters of flocs were analyzed from the images by software named Image-pro Plus 6.0 (Media Cybernetics Inc., USA), and they were sequenced according to their numerical magnitude in each group. The top 50 will be used to calculate the mean value.⁶

2.3.3. Flocculating rate analysis. Flocculating activity was evaluated by flocculating rate (FR) according to eqn (2):

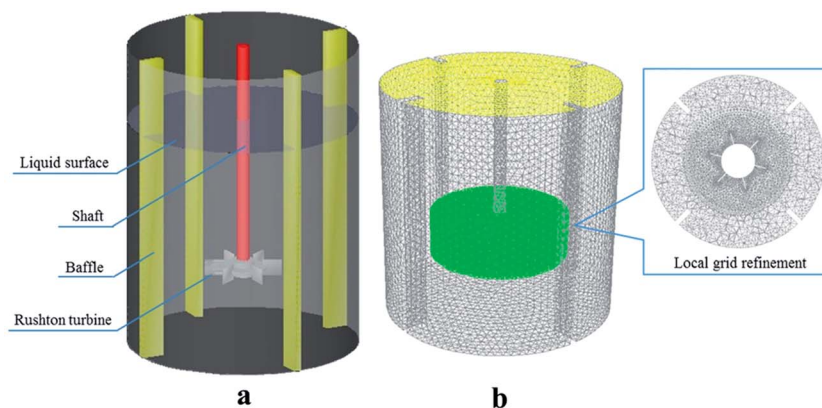


Fig. 1 Schematic of (a) geometry of the flocculation reactor; and (b) tetrahedral computational grid used for the simulation.

$$FR = (b - a)/b \times 100\% \quad (2)$$

where a and b are the optical densities (OD) of the sample and control at 550 nm, respectively. And the OD of the upper phase was measured by the spectrophotometer (7230G, Shanghai, China).

2.3.4. Turbidity and zeta potential analysis. The turbidity was measured by the turbidimeter (XZ-0101S, Shanghai, China). The variation of zeta potential during the flocculation process was monitored by Zetasizer (Nano-ZS90, Malvern, England). Samples were taken at different time points: kaolin suspension (at pH 8) without additives, after adding CaCl_2 , and after adding MBFGA1.

2.4. Methodology for CFD model generation

2.4.1. Hydrodynamic model. Mechanical mixing by the Rushton turbine in the flocculation reactor created turbulence. The standard k - ϵ model was used to account for the turbulence, which has been widely applied and validated to simulate mixing because of its simplicity, low computational requirement and good convergence for complex turbulent flows.¹⁸ Governing equations of the standard k - ϵ model for turbulent kinetic energy (k) and kinetic energy dissipation rate (ϵ) are expressed as:

$$\frac{\partial}{\partial t}(\rho k) + \frac{\partial}{\partial x_i}(\rho k u_i) = \frac{\partial}{\partial x_j} \left[\left(\mu + \frac{\mu_t}{\sigma_k} \right) \frac{\partial k}{\partial x_j} \right] + G_k - \rho \epsilon \quad (3)$$

$$\frac{\partial}{\partial t}(\rho \epsilon) + \frac{\partial}{\partial x_i}(\rho \epsilon u_i) = \frac{\partial}{\partial x_j} \left[\left(\mu + \frac{\mu_t}{\sigma_\epsilon} \right) \frac{\partial \epsilon}{\partial x_j} \right] + C_{1\epsilon} \frac{\epsilon}{k} G_k - C_{2\epsilon} \rho \frac{\epsilon^2}{k} \quad (4)$$

where the turbulent viscosity, μ_t , is calculated according to: $\mu_t = \rho C_\mu k^2/\epsilon$, G_k is the generation of turbulence kinetic energy due to mean velocity gradients, σ_k and σ_ϵ are the effective Prandtl numbers for k and ϵ , respectively. The empirical model constant values are generally accepted as $C_\mu = 0.09$, $C_{1\epsilon} = 1.44$, $C_{2\epsilon} = 1.92$, $\sigma_k = 1.0$ and $\sigma_\epsilon = 1.3$.

Simulating mechanical mixing in the reactor requires that the model should be divided into a rotating zone, as shown in green color in Fig. 1(b), and a stationary zone, as shown in gray color in Fig. 1(b). The inner zone includes the impeller which is

responsible for the motion of fluid in the reactor. The outer zone without moving parts is passively driven by the impeller. To ensure a precise modeling of the impeller effect on the hydrodynamic behavior, a steady-state modeling method called multiple reference frames (MRFs) was employed as it provided accurate prediction and demanded less computational resource.²⁰

2.4.2. Numerical considerations. In this work, the full computational geometry and tetrahedral unstructured grid, shown in Fig. 1(b), were generated for CFD calculations to capture more accurate results. The grid-independent test was conducted to determine the minimum grid resolution that achieved a solution independent of the mesh quantities. Three different mesh sizes including (a) 158 322 (coarse mesh), (b) 323 910 (fine mesh) and (c) 899 355 (very fine mesh) were evaluated using the mean velocity magnitude. Difference of mean velocity between case (a) and (b) was 16.5%, while this difference between case (b) and (c) was only 1.2%. As a result, the grid of 323 910 cells was selected for the simulation.

The water-free surface, shown in yellow color in Fig. 1(b), was modeled as a fixed surface, and this plane of symmetry was characterized by zero normal gradients for all variables. No-slip boundary conditions were imposed on all wall surfaces. The method to judge convergence was to monitor the magnitudes of scaled residuals, which were defined as the imbalance in each conservation equation following the iteration. The solutions were said to have converged when the scaled residuals went below values of 10^{-4} .

3. Results and discussion

3.1. Effect of flow fields on flocculation performance

An analysis of experimental results indicated the effect of flow fields in the reactor on flocculation performance of MBFGA1.

3.1.1. Characterization of flow fields. Flow fields in the reactor were generated by the Rushton turbine at different impeller speeds during the flocculation process. G (s^{-1}), the average shear rate throughout the reactor, is now used worldwide to characterize the global flow field, which is calculated as follows:²¹

$$G = (\varepsilon_{\text{ave}}/\nu)^{1/2} \quad (5)$$

where ν is the kinematic viscosity of the suspending fluid and ε_{ave} is the average turbulent energy dissipation rate, which was given by:²²

$$\varepsilon_{\text{ave}} = N_p N^3 D^5 / V \quad (6)$$

where N_p is the impeller power number (here for the Rushton turbine, $N_p = 5$),²³ N is the impeller speed, and V is the stirred tank volume.

In addition, an estimate of the frequency of exposure of the particles to the high shear impeller zone can be obtained from the circulation time, T_c , presented as:

$$T_c = V / (N_q N D^3) \quad (7)$$

where N_q is the dimensionless impeller pumping capacity: for the Rushton turbine $N_q = 0.9$.²³

Table 1 showed the average shear rate (G) and circulation time (T_c) at the different impeller speeds of rapid mixing and slow mixing. As the rapid mixing speed increased from 200 rpm to 600 rpm, the value of G got an increase of 420%, while the value of T_c was just decreased by 66%. However, increasing the slow mixing speed from 50 rpm to 100 rpm made the value of T_c decrease by 50%, under the condition of which the value of G was just increased by 178%. Consequently, at the stage of slow mixing, the change in the value of G made bigger differences in the value of T_c , that is to say the frequency of exposure of the particles to the high shear zone was more related to the flow field generated by slow mixing. The use of the constant G and T_c offered a good basis for characterization of small reactors such as the lab-scale flocculation reactor used here, which was consistent with previous works of Spicer *et al.*²³

3.1.2. Effect of rapid mixing on flocculation performance.

In flocculation tests, rapid mixing of kaolin suspension was carried out to guarantee homogeneous dispersion of CaCl_2 solution and MBFGA1 fermentation liquid. The CaCl_2 solution provided Ca^{2+} for the flocculation process as a kind of coagulant aid which decreased the negative charge of the kaolin particles and charge neutralization occurred immediately after the addition of Ca^{2+} .⁶ The active species, *i.e.* Ca^{2+} -kaolin complexes, formed by the reactions promoted the destabilization of kaolin suspension and the collision between suspended particles and MBFGA1 was also enhanced through high shear flow. Table 2 showed the effect of rapid mixing on flocculation performance. The initial pH was 8, and the slow mixing was 80 rpm. The maximum decrement of zeta potential from -48.45 ± 0.64 mV to -14.48 ± 0.12 mV was achieved at $G = 402 \text{ s}^{-1}$ ($N = 400$ rpm).

Zeta potential of the sample can determine whether the particles tend to flocculate or not in the liquid, and the more closely zeta potential gets to zero, the more beneficially flocculation occurs.²⁴ Therefore, it can be seen in Table 2 that the best final flocculation efficiency, *i.e.* 3.03 ± 0.10 NTU for the lowest residual turbidity and $98.2 \pm 0.8\%$ for the highest flocculating rate, was also achieved at $G = 402 \text{ s}^{-1}$.

In the case of charge neutralization, rapid mixing is especially important since poor mixing can lead to local overdosing and restabilization of some particles. MBFGA1 dispersed slowly under the condition of low shear rate, such as $G = 142 \text{ s}^{-1}$ ($N = 200$ rpm) and $G = 261 \text{ s}^{-1}$ ($N = 300$ rpm). As a result, the collision probability between MBFGA1 and suspended particles was relatively low with a few primary aggregates of poor quality generated. On the contrary, high shear rate, *i.e.* $G = 562 \text{ s}^{-1}$ ($N = 500$ rpm) and $G = 739 \text{ s}^{-1}$ ($N = 600$ rpm), could cause damage to the primary aggregates, which had adverse influence on aggregates to further grow up in the subsequent slow mixing stage. Therefore, rapid mixing had a strong influence on final results of flocculation, which was also found in the previous research of Rossini *et al.*¹² Their bench-scale studies evaluating the optimization of rapid mixing parameters showed that turbidity removal performance was considerably improved by optimization. Dharmappa *et al.* claimed that the most important parameters for the whole optimization of flocculation were the rapid mixing parameters.²⁵ Based on the above analysis, 400 rpm ($G = 402 \text{ s}^{-1}$) was chosen as the rapid mixing speed throughout this work.

3.1.3. Effect of slow mixing on flocculation performance.

Followed by rapid mixing at 400 rpm, slow mixing at six different impeller speeds was allowed for 10 min. After the flocculation process, the flocculation performance of MBFGA1 was evaluated by the mean floc size, residual turbidity and flocculating rate as shown in Fig. 2. The addition of MBFGA1 and Ca^{2+} brought about a change in the nature of small kaolin suspended particles, rendering them unstable, whilst flocculation encouraged particle agglomeration *via* gentle mixing and the formation of irregularly-shaped, loosely-connected mass fractal aggregates, known as flocs.²⁶ In Fig. 2, flocs mixed at speeds less than 80 rpm ($G = 36 \text{ s}^{-1}$) exhibited an increase in size when the speed accelerated. And in these instances, the modest inertial increases emerged when the shear rate was up, making the floc size jump from about $486 \mu\text{m}$ to $538 \mu\text{m}$ and causing the small degree of breakage. The floc was observed to diminish in size from about $538 \mu\text{m}$ to $496 \mu\text{m}$, when mixed at speeds in excess of 80 rpm ($G = 36 \text{ s}^{-1}$). Jarvis *et al.* also reported that the kaolin flocs demonstrated a constant rate of

Table 1 Average shear rate (G) and circulation time (T_c) at different impeller speeds

Characterized parameters	Rapid mixing (rpm)					Slow mixing (rpm)					
	200	300	400	500	600	50	60	70	80	90	100
$G (\text{s}^{-1})$	142	261	402	562	739	18	23	29	36	43	50
$T_c (\text{s})$	7.1	4.7	3.5	2.8	2.4	28.3	23.6	20.2	17.7	15.7	14.1

Table 2 Effect of rapid mixing on flocculation of kaolin suspension

Average shear rate G (s^{-1})	Zeta potential (mV)			Residual turbidity (NTU)	Flocculating rate (%)
	Without additives	After adding Ca^{2+}	After adding MBFGA1		
142	-48.45 ± 0.64	-21.27 ± 0.15	-22.12 ± 0.14	8.56 ± 0.14	85.7 ± 1.8
261	-48.45 ± 0.64	-19.32 ± 0.16	-21.04 ± 0.07	7.89 ± 0.21	86.8 ± 2.3
402	-48.45 ± 0.64	-13.96 ± 0.09	-14.48 ± 0.12	3.03 ± 0.10	98.2 ± 0.8
562	-48.45 ± 0.64	-15.81 ± 0.14	-16.41 ± 0.08	4.25 ± 0.18	93.6 ± 0.8
739	-48.45 ± 0.64	-16.20 ± 0.13	-16.63 ± 0.12	6.47 ± 0.11	90.5 ± 1.2

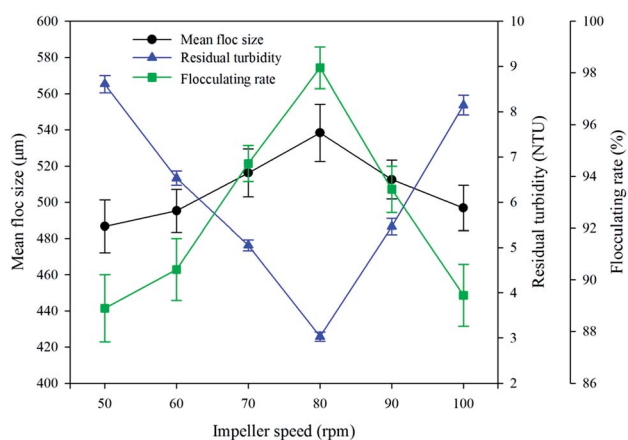


Fig. 2 Effect of the slow mixing speed on flocculation performance of MBFGA1.

degradation upon exposure to increased mixing speeds (and so increased shear rate).²⁷

Flocs grew initially at a rate that was determined mainly by the applied shear. Table 1 showed that when the impeller of the reactor rotated at different speeds ($N = 50$ – 100 rpm), flocs were exposed to a range of shear rate ($G = 18$ – 50 s^{-1}). Moreover, the circulation time, T_c , was decreased from 28.3 s to 14.1 s as the shear rate increased, which increased the frequency of exposure of flocs to the high shear zone. As a result, the flocs breakage frequency was also increased. As flocs became larger, further growth was restricted by the applied shear. In order to resist the breakage, flocs must be able to withstand shear energy applied to them in the flocculation reactor. But when the degree of shear exceeded a threshold value, flocs breakage occurred until a new steady state was reached.²⁸ A dynamic balance between floc growth and breakage led to a steady-state floc size distribution. Therefore, the constant floc size distribution was found under the given shear conditions in Fig. 2, demonstrating a trend of increasing first and then decreasing.

In an operational sense, the floc size causes a critical effect on the solid/liquid separation process. Small flocs generally settle more slowly than larger flocs of similar density, which leads to a lower particles removal efficiency.²⁹ Yu *et al.* found that the residual turbidity after settling was mainly determined by the small flocs, and the lower the frequency of small flocs, the lower the residual turbidity.¹⁴ Consequently, it can be seen in Fig. 2 that the floc size was consistent with the relative

residual turbidity and flocculating rate, *i.e.* the larger the flocs were, the better they settled resulting in lower residual turbidity and higher flocculating rate. Both the lowest residual turbidity (3.03 ± 0.10 NTU) and the maximum flocculating rate ($98.2 \pm 0.8\%$) were achieved at the impeller speed of 80 rpm ($G = 36$ s^{-1}).

The results of flocculation tests demonstrated that the hydrodynamic environment of the reactor, induced by rapid mixing at 400 rpm ($G = 402$ s^{-1}) then slow mixing at 80 rpm ($G = 36$ s^{-1}), was the most efficient for flocculation. Like other flocculating factors, the mixing conditions should also be optimized, and MBFGA1 showed a talented flocculating capability for kaolin suspension under the conditions of the suitable flow fields in the flocculation reactor.

3.2. CFD simulation

In principle the mixture of water with flocs in the flocculation reactor should be treated as a two-phase flow mathematical problem. Nevertheless, according to the experimental observation the volume fraction of the dispersed phase (flocs) was less than 5%, and therefore, it could be safely assumed that the presence of the flocs did not affect the flow field. Furthermore, the size and density of the flocs were such that their Stokes numbers (St) were much less than 1. For $St \ll 1$, the flocs will closely follow the flow field, which implies that there is no need to consider flocs as a second phase.³⁰ From the above analysis, the simulation can adopt the single-phase flow model to represent the mixture reducing the computational effort. Six steady state simulations, at the impeller speeds from 50 rpm to 100 rpm at the interval of 10 rpm, were conducted. The velocity field, local shear rate, and turbulent kinetic energy were evaluated in certain planes passing through the reactor.

3.2.1. Model verification. The profiles of the mean radial and tangential velocities normalized with the impeller tip velocity (U_{tip}) were plotted in Fig. 3 at the impeller discharge boundary ($r/R = 1.07$). As far as the CFD model validity was concerned, the velocity components were compared with results of earlier works.^{31,32} If the numerical errors and the measurement inaccuracies were taken into consideration, the CFD simulated results were in reasonable agreement with the measurements. The relative error between the simulated and measured data was within 10% indicating that the present model provided a good overall description of the flow behaviors in the flocculation reactor.

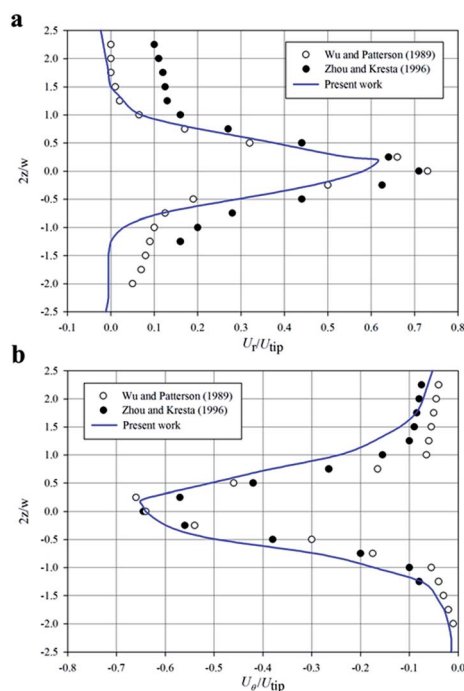


Fig. 3 Comparison between the simulated and experimental profiles of (a) the normalized radial velocity U_r/U_{tip} ; and (b) the normalized tangential velocity U_θ/U_{tip} at $r/R = 1.07$ (z , w , and r represent axial coordinate, impeller blade width and radial coordinate, respectively).

3.2.2. Visualization of flow fields. To gain an insight into the flow pattern in the flocculation reactor, taking the case of the rapid mixing at 400 rpm ($G = 402 \text{ s}^{-1}$) as an example, the flow pathlines colored by the velocity magnitude released from the impeller and the global velocity vectors in the vertical plane midway between two baffles were depicted in Fig. 4. The well-known two-loop flow pattern, characteristics of the radial flow impeller, can be clearly identified. The liquid agitated by the impeller travelled towards the radial direction and then split

into two streams near the wall of the reactor. One stream above the impeller created an upward circulation loop near the surface of the mixture; the other below the impeller created a downward circulation loop towards the bottom of the reactor. Under this rapid mixing condition, MBFGA1 and Ca^{2+} could be dispersed as quickly as possible. The left contour bar represented the velocity scales ranging from zero (blue area) to the maximum value (red area) in which the velocity magnitudes were greater than (or equal to) the maximum value specified. These representations can be approximately applied to all the contour figures in this study. The 3-D visualization of the flow pathlines showed a high velocity along the impeller discharging direction, while a low velocity emerged near the wall, which corresponded to the velocity contours presented in Fig. 5. The global velocity contours in the vertical plane midway between two baffles with respect to six impeller speeds were given in Fig. 5. From this figure, it can be observed that all the flow patterns were symmetrical to the centrally-located shaft and the highest velocities were limited within the paddle tip zone. The velocity of the mixture was found to increase with increase in the impeller speed. Area-weighted average of velocity magnitudes in the plane at six impeller speeds from 50 rpm to 100 rpm were 0.0138, 0.0170, 0.0203, 0.0235, 0.0268 and 0.0302 ms^{-1} , respectively. Changes to the slow mixing speed did impose a significant impact on the local velocity magnitude distribution. The uniformity of velocity distribution was achieved as the impeller speed increased, and a well-proportioned velocity magnitude, such as the case of $N = 80$ rpm, meant effective use of the volume of the reactor for flocculation.

In theory, the average shear rate (G) shown in Table 1 can be used to characterize the global flow field in the flocculation reactor. In practice, however, the flow characteristics vary within the reactor from point to point and it's flawed to represent a complex flow field within a single number. Consequently, it is important to describe the fluctuations adequately in local shear to which the flocs were subjected. Fig. 6 displayed the local

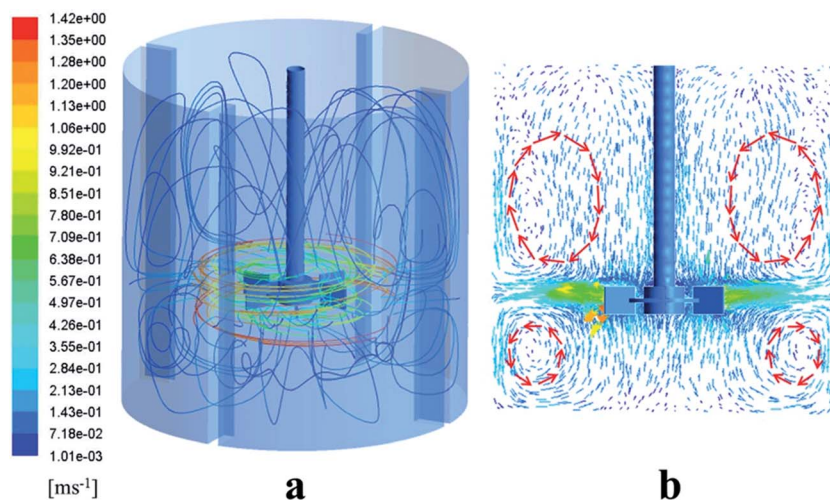


Fig. 4 Flow pattern at the rapid mixing speed of 400 rpm: (a) pathlines colored by velocity magnitude; and (b) velocity vectors in the vertical plane.

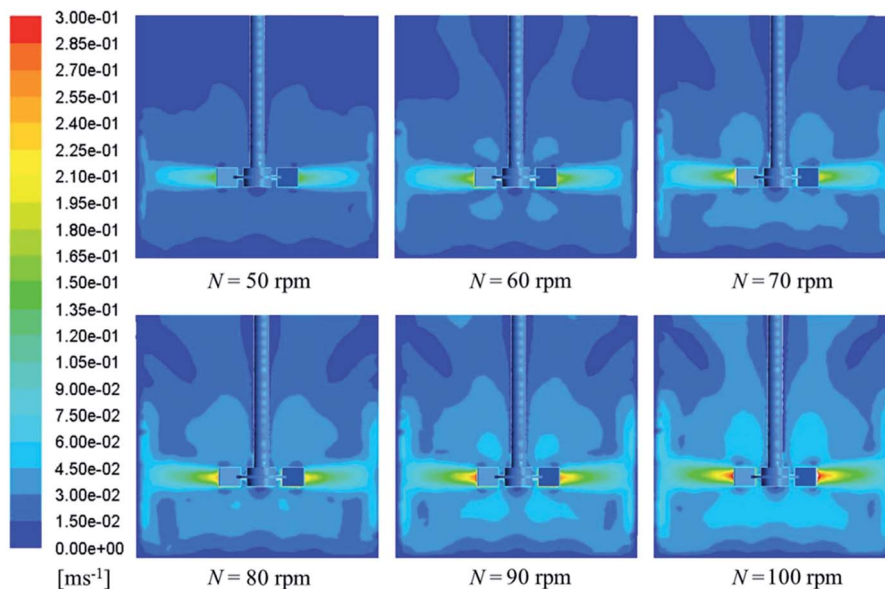


Fig. 5 Velocity contours in the vertical plane midway between two baffles.

shear rate (G_L) contours of four horizontal planes across the reactor. The four planes were orderly named by plane 1, plane 2, plane 3 and plane 4 from top to bottom. Each plane was at an interval of 40 mm along the vertical direction and plane 4 was 10 mm above the bottom. It can be seen that the value of G_L in plane 1 and plane 2 were all below 10 s^{-1} and nearly unchanged with variation in the impeller speed except for areas near the wall. While obvious changes in the value of G_L in plane 3 and plane 4 could be clearly observed. It was evident that the fluid hydraulic shear stress in the areas across or below the impeller was higher than that in the areas above the impeller. Especially,

the impeller zone owned the highest fluid hydraulic shear stress in the reactor. Areas of high value of G_L were also typically areas where the highest mixing existed, but the associated high shear stress could cause damage to flocs, and should be avoided.¹⁶ When the flocs were subjected to an increased shear rate, breakage would occur. Furthermore, the short circulation time resulting from increasing shear rate increased the frequency of exposure of the flocs to the high intensity shear in the impeller zone (Table 1). The flocs size decreased obviously when slow mixing speed exceeded the threshold value, *i.e.* 80 rpm (Fig. 2). Proper controlling of the shear rate undoubtedly becomes

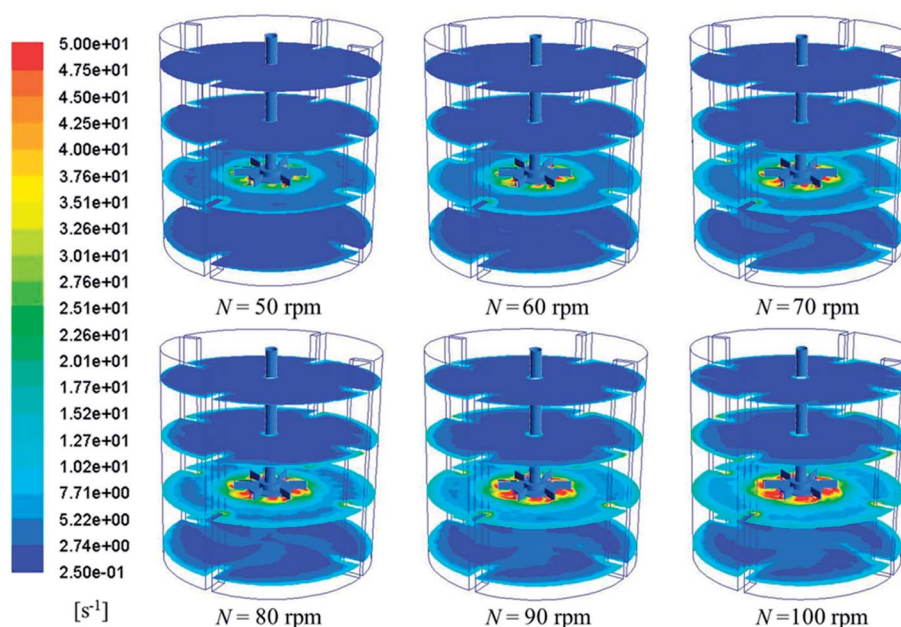


Fig. 6 Local shear rate contours in four horizontal planes across the flocculation reactor.

crucial for the efficient operation of flocculation. Integrating the results in Section 3.1.3 with CFD predictions, it can be concluded that the G_L at the impeller speed of 80 rpm not only satisfied the optimum hydrodynamic conditions of flocs growth for flocculation but also guaranteed the small degree of damage to flocs.

After the two stages of mixing, gravity settlement of the flocs was sustained for 30 min. Fig. 7(a) showed the distribution of flocs accumulation at the bottom of the reactor after the settlement procedure, from which it was found that the uniformity of flocs accumulation distribution was improved with an increasing impeller speed. This can be explained by the distribution of turbulent kinetic energy (k) in the horizontal plane (3 mm above the bottom) shown in Fig. 7(b). It can be seen that with an increase in the impeller speed, the value of k at the bottom of the reactor went up and uniformity of the k distribution was achieved. According to the two-loop flow pattern in the reactor shown in Fig. 4, a part of the energy supplied by the impeller, which was associated with the lower

loop, was available in the bottom region for performing various functions such as flocs suspension. Since all the energy given to the fluid was converted to k , the regions with higher value of k were more beneficial for flocs suspension, and the regions with lower value of k were easier for flocs sedimentation.³³ In Fig. 7(b), k with the value of $2.73 \times 10^{-5} \text{ m}^2 \text{ s}^{-2}$ was the least possible to promote flocs suspension at this plane. As a result, the flocs would not likely to settle down to the bottom during the flocculation process at a relatively high impeller speed, such as 80, 90 and 100 rpm, until the mixing procedure came to the end. Hence, the flocs collision frequency could be enhanced by flocs suspension at a suitable impeller speed (80 rpm) resulting in an improved level of flocs growth. Moreover, Fig. 7 showed that the shapes of the simulated turbulent kinetic energy contours and the distribution of flocs accumulation were similar at the corresponding impeller speed, once again demonstrating that the simulated results were acceptable.

The analysis was performed using conventional and typical CFD software, readily available to the practicing engineer, and

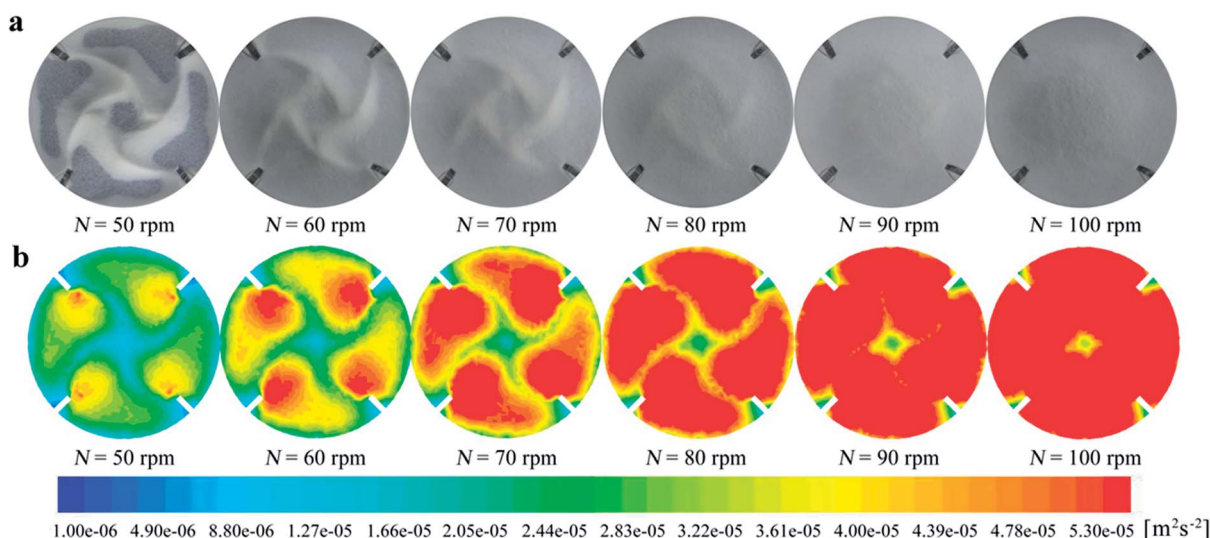


Fig. 7 (a) Distribution of flocs accumulation; and (b) turbulence kinetic energy contour in the horizontal plane.

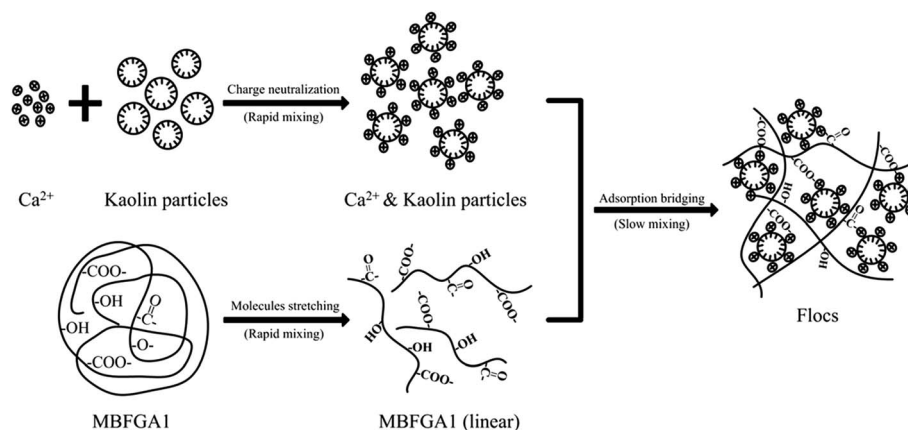


Fig. 8 Proposed flocculation mechanisms of MBFGA1.

its completion was significantly more efficient than post-construction field tests. According to the results of CFD simulations and flocculation tests, a qualitative and quantitative relationship between flow fields and flocculation efficiency of MBFGA1 can be obtained.

3.3. Mechanism of flocculation

As shown in Table 2, the zeta potential of kaolin suspension (at initial pH 8) was -48.45 ± 0.64 mV. After adding Ca^{2+} , it turned to be -13.96 ± 0.09 mV (at $G = 402 \text{ s}^{-1}$). Addition of MBFGA1 to kaolin suspension had negative effects on reducing the surface charge of kaolin particles. This was due to the fact that both the MBFGA1 fermentation (-16.9 ± 0.12 mV) and kaolin suspension were negatively charged. Therefore, charge neutralization was achieved by the addition of Ca^{2+} during the process of rapid mixing. Ca^{2+} could increase the initial adsorption capacity of MBFGA1 by decreasing the negative charge on both the polymer and the particle. It also reduced the absolute values of zeta potential in the flocculation system, which was consistent with the results of some researchers.^{5,6} In addition, MBFGA1 had a linear long chain molecular structure mainly composed of rhamnose, xylose, mannose, galactose, glucose, and appeared to have a molecular weight of 1.18×10^6 Da.³⁴ It could seize OH^- from kaolin suspension at pH 8 competitively, making the molecules stretch to form a linear structure so that more of the active binding sites emerged.⁵ These interactions were promoted by rapid mixing accompanied with the high shear rate ($G = 402 \text{ s}^{-1}$). During the process of slow mixing, MBFGA1 acted like a bridging agent of Ca^{2+} -kaolin complexes formed in the rapid mixing stage. Many Ca^{2+} -kaolin complexes were absorbed onto the long molecular chains, and they could be absorbed simultaneously by other polymer chains in MBFGA1, leading to the formation of three-dimensional flocs with a better settling capacity. The slow mixing speed played an important role in this process. The best performance of flocculation occurred at 80 rpm (Fig. 2). The befitting hydrodynamic flow field allowed the aggregates to bridge two or more flocs to form larger floc particles, which increased the particle removal efficiency. The mechanisms of flocculation were presented in Fig. 8. It could be concluded that the flocculation of kaolin suspension using MBFGA1 was completed by charge neutralization occurred at the stage of rapid mixing and adsorption bridging occurred at the stage of slow mixing.

4. Conclusions

This study reported the first systematic investigation on the effect of flow fields on flocculation of kaolin suspension using MBFGA1. The flocculation tests were conducted in a fully baffled flocculation reactor and the CFD model was built to assess the flow characteristics within the reactor. By integrating flocculation tests with CFD simulations, it was shown that flow behaviors of the reactor significantly affected the flocculation capacity of MBFGA1. The impeller with different speeds generated different flow fields, and hence offered different efficiencies for flocculation. Despite the simplifications, CFD

simulations showed a good agreement with literatures. It was found that the two-loop flow pattern in the reactor guaranteed homogeneous dispersion of Ca^{2+} and MBFGA1 at the stage of rapid mixing ($N = 400$ rpm) and promoted flocs suspension resulting in an improved level of flocs growth at the stage of slow mixing ($N = 80$ rpm). Based on the experimental observations, charge neutralization and adsorption bridging were likely the main flocculation mechanisms of MBFGA1. This work also revealed the possible application of the CFD simulation to examine flow fields for flocculation of MBFGs.

Acknowledgements

This study was supported by National Natural Science Foundation of China (30970105 and 51078131).

References

- 1 H. Seki, H. Maruyama and Y. Shoji, *Biochem. Eng. J.*, 2010, **51**, 14–18.
- 2 J. Bridgeman, B. Jefferson and S. A. Parsons, *Adv. Eng. Software*, 2010, **41**, 99–109.
- 3 R. K. Chakraborti, K. H. Gardner, J. F. Atkinson and J. E. Van Benschoten, *Water Res.*, 2003, **37**, 873–883.
- 4 D. Bouyer, C. Coufort, A. Liné and Z. Do-Quang, *J. Colloid Interface Sci.*, 2005, **292**, 413–428.
- 5 J. Feng, Z. H. Yang, G. M. Zeng, J. Huang, H. Y. Xu, Y. Y. Zhang, S. M. Wei and L. K. Wang, *Bioresour. Technol.*, 2013, **148**, 414–421.
- 6 Z. H. Yang, J. Huang, G. M. Zeng, M. Ruan, C. S. Zhou, L. Li and Z. G. Rong, *Bioresour. Technol.*, 2009, **100**, 4233–4239.
- 7 J. Huang, Z. H. Yang, G. M. Zeng, M. Ruan, H. Y. Xu, W. C. Gao, Y. L. Luo and H. M. Xie, *Chem. Eng. J.*, 2012, **191**, 269–277.
- 8 Z. Zhang, S. Xia and J. Zhang, *Water Res.*, 2010, **44**, 3087–3092.
- 9 J. N. Wang, A. Li, J. X. Yang, J. H. Wang, J. B. Guo, F. Ma, S. N. Shi, S. Zhang and N. Q. Ren, *RSC Adv.*, 2013, **3**, 18414–18423.
- 10 J. Y. Guo, C. P. Yang and G. M. Zeng, *Bioresour. Technol.*, 2013, **143**, 289–297.
- 11 T. T. More, S. Yan, N. V. Hoang, R. D. Tyagi and R. Y. Surampalli, *Bioresour. Technol.*, 2012, **121**, 425–431.
- 12 M. Rossini, J. G. Garrido and M. Galluzzo, *Water Res.*, 1999, **33**, 1817–1826.
- 13 V. A. Mhaisalkar, R. Paramasivam and A. G. Bhole, *Water Res.*, 1991, **25**, 43–52.
- 14 W. Z. Yu, J. Gregory, L. Gampos and G. B. Li, *Chem. Eng. J.*, 2011, **171**, 425–430.
- 15 K. Samaras, A. Zouboulis, T. Karapantsios and M. Kostoglou, *Chem. Eng. J.*, 2010, **162**, 208–216.
- 16 J. Bridgeman, B. Jefferson and S. A. Parsons, *Chem. Eng. Res. Des.*, 2008, **86**, 941–950.
- 17 O. P. Prat and J. J. Ducoste, *Chem. Eng. Res. Des.*, 2007, **85**, 207–219.
- 18 R. N. Meroney and P. E. Colorado, *Water Res.*, 2009, **43**, 1040–1050.

- 19 J. S. Duncan, *Colloid and Surface Chemistry*, Butterworth-Heinemann, Woburn, 4th edn, 1992.
- 20 J. Y. Luo, R. I. Issa and A. D. Gosman, *Inst. Chem. Eng. Symp. Ser.*, 1994, **136**, 549–556.
- 21 T. R. Camp and P. C. Stein, *J. Boston Soc. Civ. Eng.*, 1943, **30**, 219–237.
- 22 J. C. Godfrey, F. I. N. Obi and R. N. Reeve, *Chem. Eng. Prog.*, 1989, **85**, 61–69.
- 23 P. T. Spicer, W. Keller and S. E. Pratsinis, *J. Colloid Interface Sci.*, 1996, **184**, 112–122.
- 24 E. L. Sharp, P. Jarvis, S. A. Parsons and B. Jefferson, *Environ. Sci. Technol.*, 2006, **40**, 3934–3940.
- 25 H. B. Dharmappa, J. Verink, O. Fujiwara and S. Vigneswaran, *Water Res.*, 1993, **27**, 513–519.
- 26 P. Jarvis, B. Jefferson, J. Gregory and S. A. Parsons, *Water Res.*, 2005, **39**, 3121–3137.
- 27 P. Jarvis, B. Jefferson and S. A. Parsons, *Water Sci. Technol.*, 2004, **50**, 63–70.
- 28 J. Gregory, *Water Sci. Technol.*, 2004, **50**, 163–170.
- 29 M. Boller and S. Blaser, *Water Sci. Technol.*, 1998, **37**, 9–29.
- 30 N. Raju and E. Meiburg, *Phys. Fluids*, 1995, **7**, 1241–1264.
- 31 H. Wu and G. K. Patterson, *Chem. Eng. Sci.*, 1989, **44**, 2207–2221.
- 32 G. Zhou and S. M. Kresta, *Chem. Eng. Res. Des.*, 1996, **74**, 379–389.
- 33 J. Scully and P. Frawley, *Ind. Eng. Chem. Res.*, 2011, **50**, 2331–2342.
- 34 Y. Y. Zhang, Z. H. Yang, G. M. Zeng, J. Huang, S. M. Wei and J. Feng, *China Environ. Sci.*, 2013, **33**, 278–285.